

The magnetic field in quiescent star-forming filament G16.96+0.27

QI-LAO GU (顾琦烙),^{1,*} TIE LIU (刘铁),^{1,†} ZHI-QIANG SHEN (沈志强),^{1,‡} SIHAN JIAO (焦斯汗),² JULIEN MONTILAUD,³ MIKA JUVELA,⁴ XING LU (吕行),¹ CHANG WON LEE,^{5,6} JUNHAO LIU (刘峻豪),⁷ PAK SHING LI,¹ XUNCHUAN LIU (刘训川),¹ DOUG JOHNSTONE,^{8,9} WOJIN KWON,^{10,11,12} KEE-TAE KIM,^{5,6} KEN'ICHI TATEMATSU,^{13,14} PATRICIO SANHUEZA,^{7,14} ISABELLE RISTORCELLI,¹⁵ PATRICK KOCH,¹⁶ QIZHOU ZHANG,¹⁷ KATE PATTLE,¹⁸ NAOMI HIRANO,¹⁶ DANA ALINA,^{19,20} AND JAMES DI FRANCESCO^{21,22}

¹Shanghai Astronomical Observatory, Chinese Academy of Sciences
No.80 Nandan Road, Xuhui, Shanghai 200030, People's Republic of China

²National Astronomical Observatories, Chinese Academy of Sciences
A20 Datun Road, Chaoyang, Beijing 100101, People's Republic of China

³Université de Franche-Comté, CNRS, Institut UTINAM, OSU THETA, F-25000 Besançon, France

⁴Department of Physics, PO box 64, FI-00014, University of Helsinki, Finland

⁵Korea Astronomy and Space Science Institute, 776 Daedeokdae-ro, Yuseong-gu, Daejeon 34055, Republic of Korea

⁶University of Science and Technology, Korea, 217 Gajeong-ro, Yuseong-gu, Daejeon 34113, Republic of Korea

⁷National Astronomical Observatory of Japan, 2-21-1 Osawa, Mitaka, Tokyo, 181-8588, Japan

⁸NRC Herzberg Astronomy and Astrophysics, 5071 West Saanich Rd, Victoria, BC, V9E 2E7, Canada

⁹Department of Physics and Astronomy, University of Victoria, Victoria, BC, V8P 5C2, Canada

¹⁰Department of Earth Science Education, Seoul National University, 1 Gwanak-ro, Gwanak-gu, Seoul 08826, Republic of Korea

¹¹SNU Astronomy Research Center, Seoul National University, 1 Gwanak-ro, Gwanak-gu, Seoul 08826, Republic of Korea

¹²The Center for Educational Research, Seoul National University, 1 Gwanak-ro, Gwanak-gu, Seoul 08826, Republic of Korea

¹³Nobeyama Radio Observatory, National Astronomical Observatory of Japan, National Institutes of Natural Sciences
Nobeyama, Minamimaki, Minamisaku, Nagano 384-1305, Japan

¹⁴Astronomical Science Program, Graduate Institute for Advanced Studies, SOKENDAI
2-21-1 Osawa, Mitaka, Tokyo 181-8588, Japan

¹⁵IRAP, Université de Toulouse, CNRS, 9 avenue du Colonel Roche, BP 44346, 31028 Toulouse Cedex 4, France

¹⁶Academia Sinica Institute of Astronomy and Astrophysics, No. 1, Section 4, Roosevelt Road, Taipei 10617, Taiwan (R.O.C.)

¹⁷Center for Astrophysics — Harvard & Smithsonian
60 Garden Street, Cambridge, MA 02138, USA

¹⁸Department of Physics and Astronomy, University College London, Gower Street, London WC1E 6BT, United Kingdom

¹⁹Department of Physics, School of Science and Technology, Nazarbayev University, Astana 010000, Kazakhstan

²⁰IRAP, Université de Toulouse CNRS, UPS, CNES, F-31400 Toulouse, France

²¹Department of Physics and Astronomy, University of Victoria, Victoria, BC, V8W 2Y2, Canada

²²2 NRC Herzberg Astronomy and Astrophysics, 5071 West Saanich Road, Victoria, BC, V9E 2E7, Canada

ABSTRACT

We present 850 μm thermal dust polarization observations with a resolution of 14.4'' (~ 0.13 pc) towards an infrared dark cloud G16.96+0.27 using JCMT/POL-2. The average magnetic field orientation, which roughly agrees with the larger-scale magnetic field orientation traced by the *Planck* 353 GHz data, is approximately perpendicular to the filament structure. The estimated plane-of-sky magnetic field strength is ~ 96 μG and ~ 60 μG using two variants of the Davis-Chandrasekhar-Fermi methods. We calculate the virial and magnetic critical parameters to evaluate the relative importance of gravity, the magnetic field, and turbulence. The magnetic field and turbulence are both weaker than gravity, but magnetic fields and turbulence together are equal to gravity, suggesting that G16.96+0.27 is in a quasi-equilibrium state. The cloud-magnetic-field alignment is found to have a trend moving away from perpendicularity in the dense regions, which may serve as a tracer of potential fragmentation in such quiescent filaments.

Keywords: ISM: magnetic fields — stars: formation — ISM: individual objects: G16.96+0.27

1. INTRODUCTION

Filaments are ubiquitous in the interstellar medium (e.g., Myers 2009; Arzoumanian et al. 2011; André et al. 2010) with chains of dense cores embedded (e.g., Zhang et al. 2009; André et al. 2014; Könyves et al. 2015; Tafalla & Hacar 2015; Morii et al. 2023), indicating that the filamentary structure might be an important stage in the star formation process (Liu et al. 2012; Lu et al. 2018). The details regarding how filaments fragment into dense prestellar cores and further evolve to form protostars are still under debate. Specifically, the role that the magnetic field plays during this process remains far from being fully understood (Crutcher 2012; Li et al. 2014; Pattle et al. 2023).

Recent state-of-the-art ideal magnetohydrodynamic (MHD) simulations of large-scale filamentary cloud formation and evolution (e.g., Li & Klein 2019) suggest that a strong magnetic field perpendicular to the filament can support the filamentary structure and guide gas flow along the field onto the main cloud. Observationally, Li et al. (2015) found that the magnetic field orientation does not change much over ~ 100 to ~ 0.01 pc scale in the filamentary cloud NGC6334, suggesting self-similar fragmentation regulated by the magnetic field. Within nearby Gould Belt Clouds (with distances smaller than 500 pc), the parallel-to-perpendicular trend of cloud-field alignment (the offset between the magnetic field orientation and the molecular cloud long axis) with increasing density indicates that these clouds may have formed from the accumulation of material along the field lines (Planck Collaboration Int. XXXV et al. 2016). With high-resolution submillimeter polarization observations, Liu et al. (2018a) found that in the massive infrared dark cloud (IRDC) G35.39-0.33 the magnetic field is roughly perpendicular to the densest part of the main filament but tends to be parallel with the gas structure in more diffuse regions. Soam et al. (2019) and Tang et al. (2019) found the magnetic field lines are more pinched by gravitational collapse at the core scale in the more evolved filamentary IRDC G34.42+0.24, where UC HII regions have formed. Ching et al. (2022) reported that a strong magnetic field shapes the main filament and subfilaments of the DR21 region. These results align with the simulations, suggesting that the magnetic field is dynamically important in the star formation process. However, active star formation has already occurred in

these filamentary clouds, and feedback from star formation may have changed the initial magnetic field. Therefore observations of more quiescent clouds are required to investigate the role of the magnetic field in core formation inside filaments.

G16.96+0.27 is one of the brightest filaments in the JCMT SCOPE survey (Liu et al. 2018b) and is located at a distance of 1.87 kpc, embedded with few protostellar and starless cores (Kim et al. 2020; Tatematsu et al. 2021; Mannfors et al. 2021). As shown in the upper panel of Figure 1, G16.96+0.27 has a simple filamentary structure and is dark at the infrared wavelengths. So it has not been illuminated by protostars in the infrared band, suggesting it is a quiescent filament at the very early stage of the star formation process. This makes G16.96+0.27 an ideal target to study the magnetic field at the early stage of star formation. Here we use our 850 μm JCMT/POL-2 thermal dust polarization observations towards G16.96+0.27 to investigate the properties of the magnetic field inside a quiescent IRDC.

This paper is organized as follows: in Section 2, we present our JCMT/POL-2 850 μm observations; in Section 3, we show the results from our observations and calculate the magnetic field strength; in Section 4, we discuss the equilibrium state and multiscale cloud-field alignment; and we provide a summary in Section 5.

2. OBSERVATIONS

G16.96+0.27 was observed 19 times from 2020 August to 2020 October (project code: M20BP043; PI: Tie Liu) using SCUBA-2/POL-2 DAISY mapping mode (Holland et al. 2013; Friberg et al. 2016, 2018) under Band 2 weather conditions ($0.05 < \tau_{225} < 0.08$, where τ_{225} is the atmospheric opacity at 225 GHz), with a total integration time of ~ 12.8 hr. The effective beam size is $14.4''$ at 850 μm (Mairs et al. 2021), corresponding to ~ 0.13 pc at a distance of 1.87 kpc.

The raw data were reduced using the *pol2map* routine of the STARLINK (Currie et al. 2014) package, SMURF (Chapin et al. 2013) with the 2019 August instrumental model¹, following the same procedures as described in Gu et al. (2024). The final Stokes I , Q and U maps are in units of pW with a pixel size of $4''$, and are converted into the unit of Jy beam^{-1} by applying the 850 μm flux conversion factor (FCF) of $668 \text{ Jy beam}^{-1} \text{ pW}^{-1}$ (Mairs et al. 2021). For the following analysis, we regrid these maps to a pixel size of $8''$ for a balance of good S/N level and enough data points. The rms noise levels of

* E-mail: qlgu@shao.ac.cn

† E-mail: liutie@shao.ac.cn

‡ E-mail: zshen@shao.ac.cn

¹ The details can be found in <https://www.eaobservatory.org/jcmt/2019/08/new-ip-models-for-pol2-data/>

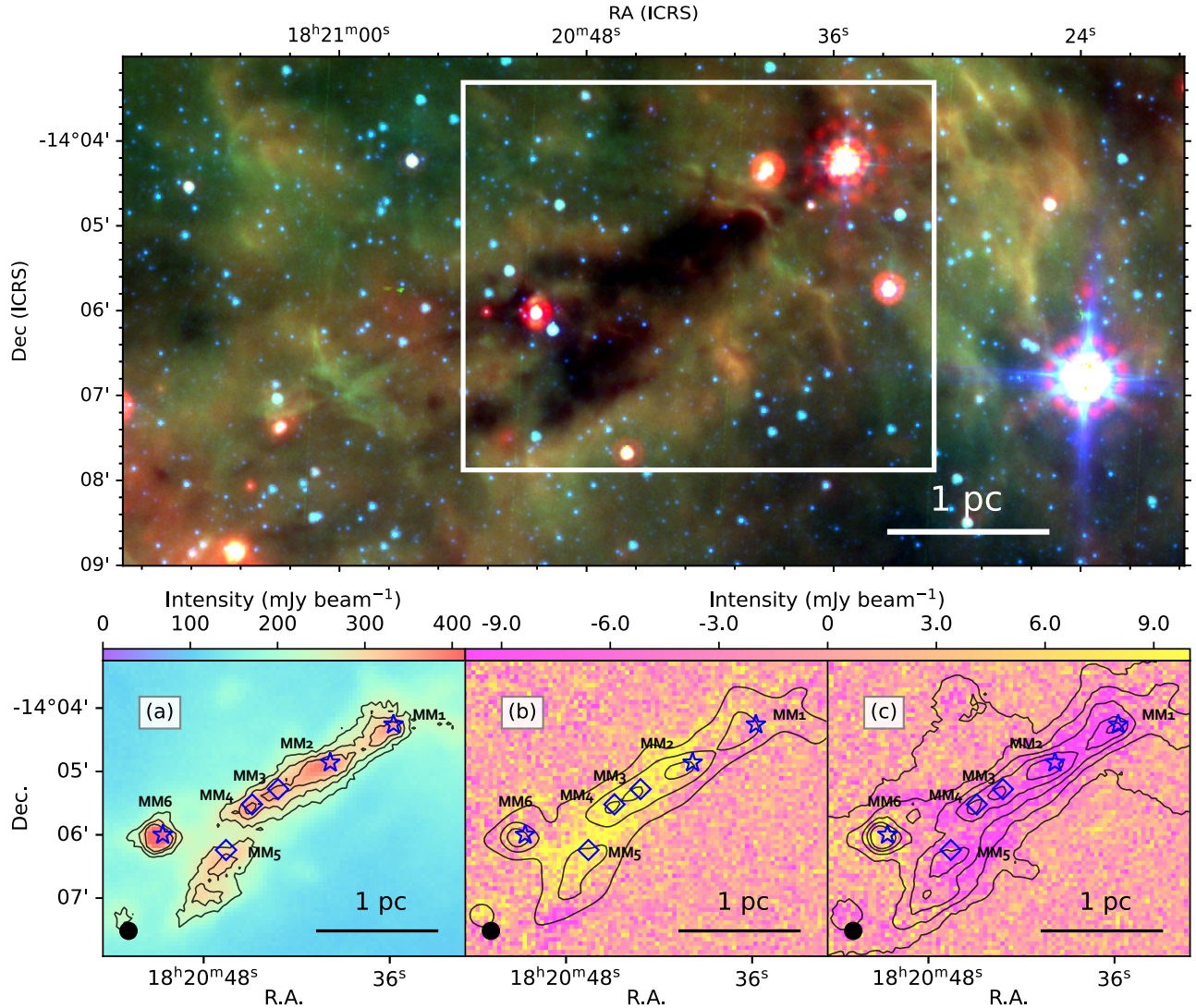


Figure 1. *Upper:* Spitzer infrared RGB map towards G16.96+0.27 (R : 24 μm ; G : 8 μm ; B : 5.8 μm). A 1-pc scale bar is shown in the lower right corner. The white box marks the region of lower panels *Lower (a-c):* JCMT/POL-2 850 μm Stokes I , Q and U maps of G16.96+0.27, and Stokes I shown here is a combination of SCUBA-2 850 μm and deconvolved Planck 353 GHz data using the J-comb algorithm (Jiao et al. 2022) considering the large scale flux. Color bars are shown on the top of the lower panels. The details can be found in Appendix B. MM1 to MM6 mark the possible fragments observed at the resolution of 14.4', star and diamond symbols represent protostellar and starless cores, respectively. Beams and the 1-pc scale bars are shown in the left and right corners, respectively. Contours in (a) show the intensity of 450 μm Stokes I at levels of [240, 480, 720] mJy beam^{-1} with an average rms noise level of 44 mJy beam^{-1} . The rms noise of the 450 μm Stokes Q and U maps is ~ 41 mJy beam^{-1} , which is not good enough for effective utilization, except in this figure, we do not show any other 450 μm results in this paper, and hereafter I , Q and U refer to 850 μm data only. Contours in (b) show the column density generated from the Herschel data by the J-comb algorithm (Jiao et al. 2022) at levels of [2.22, 3.22, 4.22] $\times 10^{22}$ cm^{-2} . Contours in (c) show the intensity of combined 850 μm Stokes I using J-comb algorithm at levels of [150, 200, 250, 300, 350] mJy beam^{-1} with an average rms noise level of 5.3 mJy beam^{-1} .

background regions are ~ 5.3 mJy beam^{-1} in the I map. and ~ 4.0 mJy beam^{-1} in the Q , U maps. The polarization information catalog is created simultaneously from these Stokes maps following the procedures as described in Appendix A. Figure 1 (b) and (c) show the final Q and U , (a) shows the final I that is combined with Planck

353 GHz flux via the J-comb algorithm (Jiao et al. 2022) as described in Appendix B.

3. RESULTS

3.1. Dust Polarization Properties and Magnetic Field Morphology

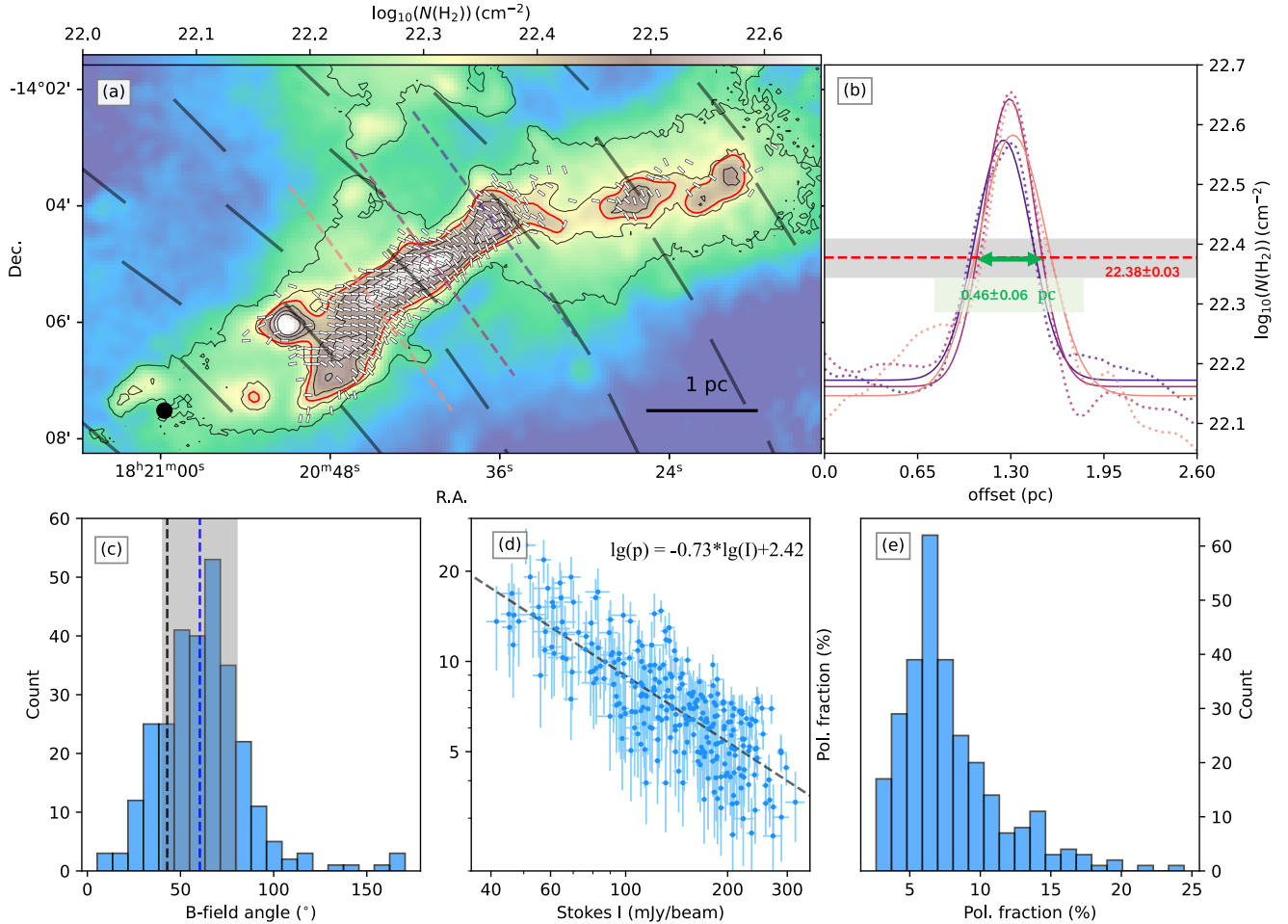


Figure 2. (a): magnetic field orientations of G16.96+0.27 overlaid on the $N(\text{H}_2)$ map with black contours showing 850 μm Stokes I levels of [150, 200, 250, 300, 350] mJy beam $^{-1}$. The short white and long black segments represent the magnetic field inferred from JCMT/POL-2 850 μm observation and Planck 353 GHz data, respectively. The 14.4'' beam size and a 1-pc scale bar are shown in the left and right lower corners. The dashed lines mark the cross-sections used for $N(\text{H}_2)$ profile fitting shown in (b), and the red contours represent the average FWHM $N(\text{H}_2)$ value of $\sim 2.39 \times 10^{22}$ cm $^{-2}$. (b): Gaussian fittings of $N(\text{H}_2)$ profiles from the three cross-sections in (a), the offset is counted from northeast to southwest. Dashed and solid lines represent the observed data and best-fitting results, respectively. The red horizontal line marks the average FWHM $N(\text{H}_2)$ and the grey region shows the uncertainty. The green double-headed arrow shows the average FWHM value of 0.46 ± 0.06 pc. (c): Distribution of magnetic field orientations, the blue dashed line represents the average value and the grey region marks the standard deviation range. The black dashed line marks the average value of magnetic field orientations inferred from Planck 353 GHz data. (d): Polarization fraction vs. initial Stokes I (not the combined one using J-comb algorithm), the dashed line shows the power-law fit, and the best-fit parameters are shown in the top right corner. (e): Distribution of polarization fraction.

The projected plane-of-sky (POS) magnetic field orientations are derived by rotating the observed polarization pseudo-vectors by 90° , based on the grain alignment assumption that the shortest axis of dust grains tends to align with the local magnetic field (Lazarian 2003). The polarization pseudo-vectors are selected by criteria of $I/\delta_I \geq 10$, $PI/\delta_{PI} \geq 3$, and $\delta_p \leq 5\%$ where δ_I is the uncertainty of Stokes I, PI and δ_{PI} are the debiased polarized intensity and the corresponding uncertainty, δ_p is the uncertainty of polarization fraction. The inferred magnetic field orientations are shown in Figure 2 (a) overlaid on the column density ($N(\text{H}_2)$)

map, which is generated from level 2.5 processed archival *Herschel* images by the J-comb algorithm as described in Appendix B (Jiao et al. 2022). The magnetic field is roughly perpendicular to the main filament structure with an average orientation of $60 \pm 20^\circ$ (Figure 2 (c)).

Figure 2 (d) shows a decreasing polarization fraction trend with increasing initial dust emission intensity fitted with a power law index of -0.73 ± 0.04 . Figure 2

² All position angles shown in this paper follow the IAU-recommended convention of measuring angles from the north towards the east.

(e) exhibits the distribution of the polarization fraction, which peaks at $\sim 6.5\%$ with a tail extending to $\sim 15\%$ – 25% . The average and median of polarization fractions are $7.8 \pm 3.6\%$, and 7.0% .

As shown in Figure 2 (a), the magnetic field is roughly perpendicular to the filament structure. In general, the small-scale ($14.4''$, ~ 0.13 pc) magnetic field traced by POL-2 agrees with the large-scale ($4.8'$, ~ 2.6 pc) magnetic field traced by *Planck*, showing similar average orientations, $60 \pm 20^\circ$ (POL-2) and $43 \pm 5^\circ$ (*Planck*). However, in the center of the filament, the small-scale magnetic field shows a $\sim 45^\circ$ difference from the large-scale one, suggesting the magnetic field orientation varies with increasing $N(\text{H}_2)$, which may reflect the effects from gravity and turbulence (see Section 4 for further discussions).

3.2. The magnetic field Strength

Before calculating the magnetic field strength, we estimate the gas density (ρ) and line-of-sight (LOS) non-thermal turbulent velocity dispersion (σ_v). As shown in Figure 2 (a-b), we choose three cross-sections to apply gaussian-fit of $N(\text{H}_2)$ profiles, and the average half maximum $N(\text{H}_2)$ is $(2.38 \pm 0.17) \times 10^{22} \text{ cm}^{-2}$ with an average FWHM $\sim 0.46 \pm 0.06$ pc. And most of the magnetic field segments are inside the contour of $N(\text{H}_2) \sim 2.38 \times 10^{22} \text{ cm}^{-2}$. Thus, we estimate the mass and ρ using the $N(\text{H}_2)$ map by assuming the filament within the $2.38 \times 10^{22} \text{ cm}^{-2}$ contour as a cylinder with a length of $\sim 2.70 \pm 0.20$ pc and a diameter of $\sim 0.46 \pm 0.06$ pc. As shown in Figure 2 (a), there are several small red contours not conjunct with the main structure and lack magnetic field segments, so we do not count them in for further calculations. Also, the protostellar core MM6 has the highest $N(\text{H}_2)$ and strong $\text{N}_2\text{H}^+(J = 1 - 0)$ (Figure 3 (a)) emission but lacks magnetic field segments, so we mask MM6 to avoid bias when estimating the mass and the velocity dispersion as well. The mass and density are then calculated as $M \sim 868_{-118}^{+116} M_\odot$ and $\rho \sim 1.31 \times 10^{-19} \text{ g cm}^{-3}$, respectively, and further the line mass $M_l \sim 321 \pm 43 M_\odot \text{ pc}^{-1}$. The corresponding volume density (n_{H_2}) is derived as $\sim 2.80 \times 10^4 \text{ cm}^{-3}$ from $\rho = \mu_{\text{H}_2} m_{\text{H}} n_{\text{H}_2}$, where $\mu_{\text{H}_2} \simeq 2.8$ is the molecular weight per hydrogen molecule (Kauffmann et al. 2008), m_{H} is the atomic mass of hydrogen.

We fit the FWHM line width, Δv , by hyperfine structure line fitting based on Nobeyama 45-m $\text{N}_2\text{H}^+(J = 1 - 0)$ data (Figure 3 (a-c), adopted from Tatematsu et al. 2021) with a resolution of $18''$. The average σ_v is then derived as $\sim 0.52 \text{ km s}^{-1}$ from $\Delta v / \sqrt{8 \ln(2)} = \sqrt{\sigma_{\text{th}}^2 + \sigma_v^2}$, where $\sigma_{\text{th}} = \sqrt{\frac{k_{\text{B}} T}{m_{\text{N}_2\text{H}^+}}}$ is the thermal velocity dispersion of N_2H^+ , k_{B} is the Boltzmann con-

stant, $m_{\text{N}_2\text{H}^+} \sim 4.85 \times 10^{-26} \text{ kg}$ is the molecular mass of N_2H^+ , T is the dust temperature (the average value is ~ 17.4 K with a standard deviation of ~ 0.6 K) derived when generating the $N(\text{H}_2)$ map by using the J-comb algorithm (Jiao et al. 2022). It is worth noting that as shown in Figure 3 (d), σ_v shows a bimodal distribution with peaks of $\sim 0.18 \text{ km s}^{-1}$ and $\sim 0.88 \text{ km s}^{-1}$, and the larger ones appear in the transition areas between the two velocity peaks shown in Figure 3 (b), which may be a signature of two velocity components. If so, σ_v is likely to be overestimated by a factor of 2 to 3. However, considering the data quality is insufficient for a deeper analysis, we still apply the average value $\sim 0.52 \text{ km s}^{-1}$ as σ_v . This may result in an overestimation of the strength of the magnetic field in the following analyses.

We apply the Davis–Chandrasekhar–Fermi (DCF) method (Davis 1951; Chandrasekhar & Fermi 1953a) to estimate the magnetic field strength. The DCF method relies on the following assumptions: the turbulence is isotropic; there is equipartition between the transverse turbulent magnetic field energy and kinetic energy; and the turbulent-to-ordered (B_t/B_o) or turbulent-to-total (B_t/B_{tot}) magnetic field ratio can be traced by the statistics of the magnetic field orientations. Then the ordered and total POS magnetic field strength could be estimated from

$$B_o = f_{\text{dcf}} \sqrt{4\pi\rho} \frac{\sigma_v}{B_t/B_o}, \quad (1)$$

and

$$B_{\text{tot}} = f_{\text{dcf}} \sqrt{4\pi\rho} \frac{\sigma_v}{B_t/B_{\text{tot}}}, \quad (2)$$

where f_{dcf} is the correction factor. When the ordered magnetic field is prominent, B_t/B_o and B_t/B_{tot} are usually estimated from $B_t/B_o \sim B_t/B_{\text{tot}} \sim \sigma_\theta$, where σ_θ is the angular dispersion of POS magnetic field orientations.

We note that there are many versions of the DCF method showing different ways to quantify B_t/B_{tot} more accurately (e.g. Falceta-Gonçalves et al. 2008; Cho & Yoo 2016; Liu et al. 2021). Here we use two of them to estimate the magnetic field strength for comparison and analysis: the classical DCF method (Ostriker et al. 2001), and the calibrated angular dispersion function (ADF) method (Hildebrand et al. 2009; Houde et al. 2009, 2016), a modified DCF method. Using the $f_{\text{dcf}} = 0.5$ derived from the numerical models (Ostriker et al. 2001) and the estimated σ_θ of $20 \pm 1^\circ$, we obtain $B_{\text{dcf}} \sim 0.5 \sqrt{4\pi\rho} \sigma_v / \sigma_\theta \sim 96 \pm 17 \mu\text{G}$.

Liu et al. (2021) calibrated the ADF method and found it accounts for the ordered magnetic field structure and beam smoothing. The turbulent correlation

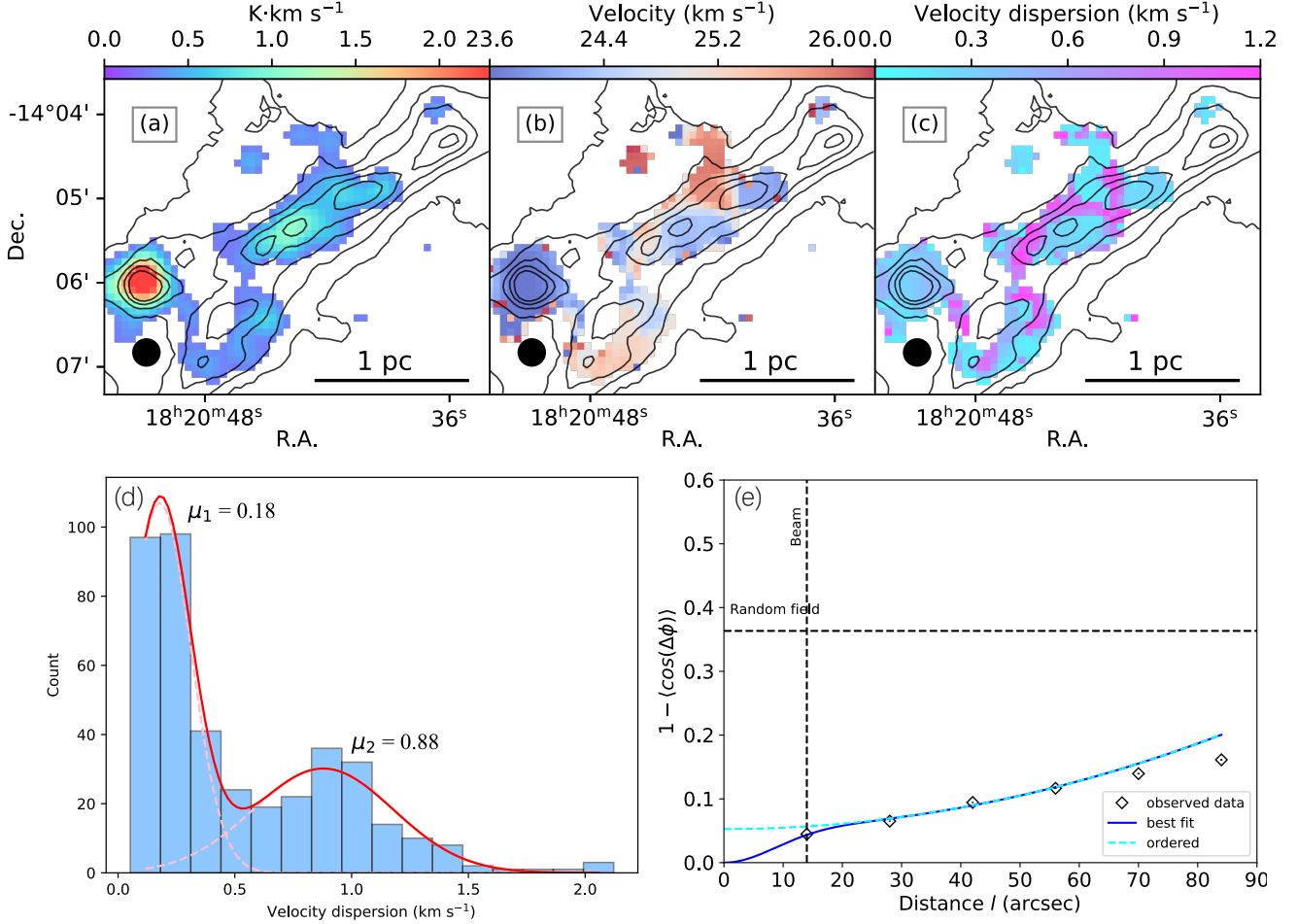


Figure 3. (a): Integrated line emission of the isolated hyperfine component of N_2H^+ with an S/N higher than 3. (b): Centroid velocity map of N_2H^+ . (c): Non-thermal velocity dispersion of N_2H^+ . Contours in (a-c) are the 850 μm Stokes I levels of [150, 200, 250, 300, 350] mJy beam $^{-1}$, the 18'' beam size and a 1-pc scale bar are shown in the left and right lower corners, respectively. (d): Distribution of the velocity dispersion shown in (c). The red curve shows the best fitting of the bimodal distribution with peaks of ~ 0.18 km s $^{-1}$ and ~ 0.88 km s $^{-1}$, dashed curves represent the two single gaussian fittings. (e): ADFs of G16.96+0.27. The diamond symbols represent the observed data points. Blue and cyan lines indicate the best-fitted result and the large-scale component of the best fit, respectively. The horizontal line marks the ADF value of a random field (0.36, Liu et al. 2021).

effect is derived from

$$1 - \langle \cos[\Delta\Phi(l)] \rangle \simeq \frac{\langle B_t^2 \rangle}{\langle B^2 \rangle} \times (1 - e^{-l^2/2(l_\delta^2 + 2W^2)}) + a_2' l^2, \quad (3)$$

where $\Delta\Phi(l)$ is the angular difference of two magnetic field angles separated by a distance of l , l_δ is the turbulent correlation length for local turbulent magnetic field, $W = l_{\text{beam}}/\sqrt{8 \ln 2}$ is the standard deviation of the Gaussian beam size and the second-order term $a_2' l^2$ is the first term of Taylor expansion of the ordered component of ADF. Figure 3 (e) shows the ADF of G16.96+0.27, we fit ADF by reduced χ^2 minimization with the best-fitted $(\langle B_t^2 \rangle / \langle B^2 \rangle)^{0.5}$ of 0.23, thus by using $B \sim 0.21 \sqrt{4\pi\rho\sigma_v} (\langle B_t^2 \rangle / \langle B^2 \rangle)^{-0.5}$ (Liu et al. 2021), we obtain $B_{\text{adf}} \sim 60 \pm 10 \mu\text{G}$. Thus, we estimate an av-

erage strength of $B_{\text{pos}} = 0.5(B_{\text{dcf}} + B_{\text{adf}}) \sim 78 \pm 20 \mu\text{G}$ for further analysis.

4. DISCUSSION

As G16.96+0.27 has a relatively simple filamentary shape, for further analysis, we identify the skeleton of this structure by applying the FilFinder algorithm (Koch & Rosolowsky 2015) to the $N(\text{H}_2)$ map. As shown in the upper panel of Figure 4, we mask MM6 when finding the skeleton for the reasons mentioned in Section 3.

4.1. Equilibrium State

For an unmagnetized filamentary cloud, the virial mass per unit length is $M_{\text{vir},l} = 2\sigma_{\text{tot}}^2/G$ (Fiege &

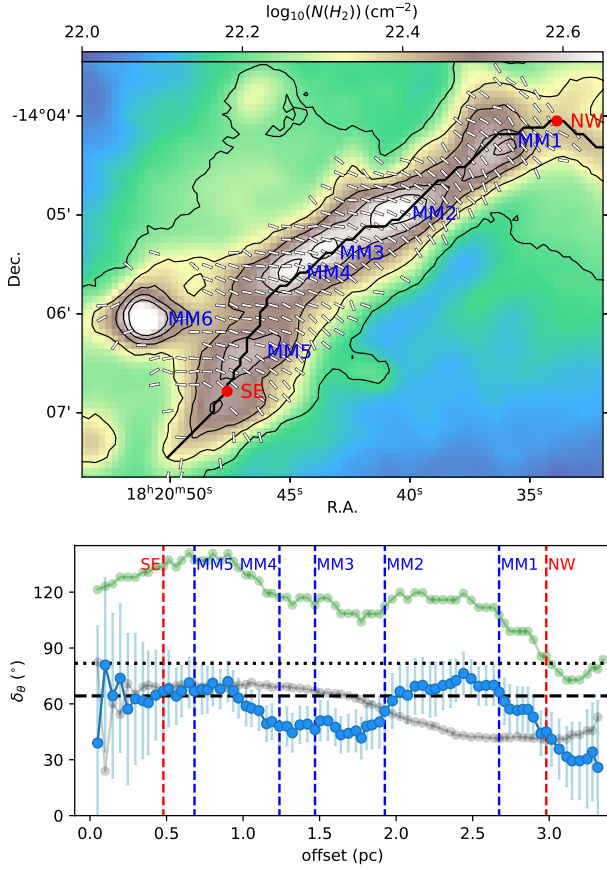


Figure 4. *Upper:* magnetic field orientation map overlaying the $N(\text{H}_2)$ map with contours showing $850\ \mu\text{m}$ Stokes I levels of $[150, 200, 250, 300, 350]\ \text{mJy beam}^{-1}$. The black curve shows the filament skeleton derived from FilFinder. The two red points mark the two ends of the skeleton. The four fragments are marked as MM1-6. *Lower:* The filament skeleton and magnetic field angle difference. The blue curve shows the angle difference between the local magnetic field and the filament skeleton, the offset is counted from the southeast to the northwest of the skeleton. The grey and green curves are the magnetic field orientation and filament orientation along the skeleton, respectively. The dashed black line marks the angle difference between the mean filament skeleton orientation and the mean POL-2 magnetic field orientation, 65.7° . In contrast, the dotted black one shows the angle difference between the mean filament skeleton orientation and the mean Planck magnetic field orientation, 81.8° . The two red dashed lines mark the locations of the two endpoints in the upper panel and the four blue dashed lines mark the locations of MM1-5.

(Pudritz 2000), where $\sigma_{\text{tot}} = \sqrt{c_s^2 + \sigma_v^2}$ is the total velocity dispersion, $c_s = \sqrt{\frac{k_B T}{\mu_p m_H}} \simeq 0.25\ \text{km s}^{-1}$ is the isothermal sound speed with an average T of $\sim 17.4\ \text{K}$ and $\mu_p \simeq 2.37$ is the mean molecular weight per free particle (Kauffmann et al. 2008). The virial parameter

is then defined as

$$\alpha_{\text{vir}} = \frac{M_{\text{vir},l}}{M_l} = \frac{2\sigma_{\text{tot}}^2}{GM_l}, \quad (4)$$

$M_{\text{vir},l}$ of G16.96+0.27 is $\sim 153\ M_\odot\text{pc}^{-1}$, and thus $\alpha_{\text{vir}} \sim 0.48 \pm 0.07$, suggesting that turbulence is weaker than gravity.

Taking the magnetic field into account, the maximum mass per length that the magnetic field can support against gravity is $M_{\Phi,l} = \Phi_l / (2\pi\sqrt{G})$, where Φ_l is the magnetic flux per unit length. The local magnetic stability critical parameter (Crutcher et al. 2004) is then defined as

$$\lambda = \frac{M_l}{M_{\Phi,l}} = \frac{\mu_{\text{H}_2} m_{\text{H}} N(\text{H}_2)}{B / (2\pi\sqrt{G})} \simeq 7.6 \times 10^{-21} \frac{N(\text{H}_2)}{B}, \quad (5)$$

where $N(\text{H}_2)$ is the column density in units of cm^{-2} and B is the total 3D magnetic field strength in units of μG . For G16.96+0.27, the average $N(\text{H}_2)$ is $\sim (3.10 \pm 0.52) \times 10^{22}\ \text{cm}^{-2}$, $B_{\text{pos}} \sim 78\ \mu\text{G}$, considering $B = \frac{4}{\pi} \overline{B_{\text{pos}}} \sim 99\ \mu\text{G}$ (Crutcher et al. 2004), λ is derived as $\sim 2.56 \pm 0.74$, indicating the magnetic field is also weaker than gravity. However, Crutcher et al. (2004) proposed that the observed M/Φ_l will be overestimated by up to a factor of 3 due to geometrical effects, this correction results in a lower limit of λ as $\lambda_{\text{min}} \sim 0.86 \pm 0.25$, showing a possibility of the magnetic field being stronger than gravity at some certain inclination angles.

Kashiwagi & Tomisaka (2021) found that when a filamentary cloud is supported by both a perpendicular magnetic field and thermal and turbulent motions, the maximum stable mass per unit length is $M_{\text{crit},l} \simeq \sqrt{M_{\Phi,l}^2 + M_{\text{vir},l}^2}$, which implies

$$\frac{M_l}{M_{\text{crit},l}} = \frac{1}{\sqrt{\lambda^{-2} + \alpha_{\text{vir}}^2}}. \quad (6)$$

$(M_l/M_{\text{crit},l})$ is $\sim 1.62 \pm 0.23$, suggesting magnetic field and turbulence together are weaker than gravity. However the lower limit $(M_l/M_{\text{crit},l})_{\text{min}} \sim 0.79 \pm 0.20$ if applying $\lambda_{\text{min}} \sim 0.86$, suggesting magnetic field and turbulence together are stronger than gravity. Thus, a $(M_l/M_{\text{crit},l}) \sim 1$ is more convincing, indicating G16.96+0.27 is in a quasi-equilibrium state. However, considering the magnetic field strength could be overestimated (see Section 3.2), $(M_l/M_{\text{crit},l})$ could be even larger and thus the filament is more likely to be a gravitationally bound system.

4.2. Fragmentation inside the Quiescent Filament

As shown in Figure 1 (a-c), there are several possible fragments along the filament major axis, which have

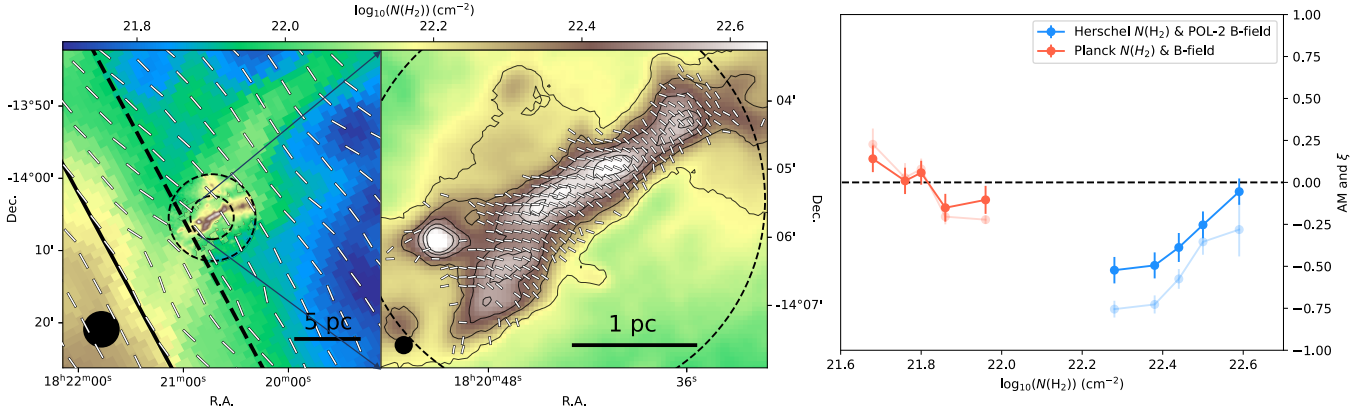


Figure 5. *Left:* column density inferred from Planck dust optical depth map at 353GHz (τ_{353}) overlaid with the one (within the outer black dashed circle) inferred from Herschel data by using the J-comb algorithm (Jiao et al. 2022). The segments show the magnetic fields derived from Planck 353 GHz polarization data, the black circle shows the beam of Planck 353GHz data with a resolution of $4.8''$, the black solid line and dashed line represent 0° and 0.185° galactic latitude, respectively. The two dashed circles mark the central regions of $12'$ and $6'$ radius, respectively. A 5-pc scale bar is shown in the lower right corner. *Middle:* column density inferred from Herschel data by using the J-comb algorithm with a resolution of $18''$ (the beam is shown in the lower left corner), overlaid segments represent the magnetic field orientation inferred from JCMT/POL-2 850 μm polarization data. The dashed circle marks the central $6'$ region, which has a useful level of coverage in the POL-2 observations. The contours show the 850 μm Stokes I levels of [150, 200, 250, 300, 350] mJy beam^{-1} . A 1-pc scale bar is shown in the lower right corner. *Right:* Alignment measure parameter AM and HRO parameter ξ calculated for the different $N(\text{H}_2)$ bins in G16.96+0.27. Red data points show the AM values (light red for ξ) inferred from Planck 353 GHz data, and blue ones show the AM values (light blue for ξ) inferred from Herschel $N(\text{H}_2)$ and POL-2 magnetic field.

been identified as protostellar (MM1, MM2 and MM6) and starless (MM3, MM4 and MM5) cores (Kim et al. 2020; Tatematsu et al. 2021; Mannfors et al. 2021). Such fragmentation can be explained by the so-called ‘sausage instability’ of a cylindrical gas structure (e.g. Chandrasekhar & Fermi 1953b; Inutsuka & Miyama 1992; Wang et al. 2014; Contreras et al. 2016). In an isothermal gas cylinder with a helicoidal magnetic field, Nakamura et al. (1993) predicted a typical spacing of fragments by

$$L \simeq \frac{2\pi}{0.72} H [(1 + \gamma)^{1/3} - 0.6]^{-1}, \quad (7)$$

where $\gamma = B_c^2 / (8\pi\rho_c\sigma^2)$, ρ_c and B_c are the density and magnetic field strength in the center, H is the scale height. According to Nakamura et al. (1993), for a cylindrical gas structure with a magnetic field of $\mathbf{B} = (0, B_\phi, B_z)$, the scale height (H) is defined from

$$4\pi G\rho_c H^2 = \sigma^2 + \frac{B_c^2}{16\pi\rho_c} (1 + \cos^2 \theta), \quad (8)$$

where $\theta = \lim_{r \rightarrow \infty} \tan^{-1} B_\phi / B_z$ denotes the ratio of B_ϕ and B_z , when $\theta = 0$, the magnetic field is parallel to the filament. $\sigma = c_s \sim 0.25 \text{ km s}^{-1}$ is the isothermal sound speed, and it is replaced by $\sigma_v \sim 0.52 \text{ km s}^{-1}$ when the fragmentation is governed by the turbulence rather than thermal Jeans instability. In G16.96+0.27, we estimated θ as the angle between the mean POS magnetic field orientation and filament skeleton ($\sim 65.7^\circ$),

and $\rho_c \sim 1.92 \times 10^{-19} \text{ g cm}^{-3}$ from $\rho_c = \frac{\rho_{\text{H}_2, \text{c}}}{n_{\text{H}_2}}$, where $n_{\text{H}_2, \text{c}} \sim 4.55 \times 10^{22} \text{ cm}^{-2}$ is the column density in the center. And we assume $B_c \sim B \sim 99 \mu\text{G}$. Therefore, we have thermal support $H_{\text{thermal}} \sim 0.04 \text{ pc}$ and turbulent support $H_{\text{turbulent}} \sim 0.05 \text{ pc}$. Further, L_{thermal} of $\sim 0.31 \text{ pc}$ and $L_{\text{turbulent}}$ of $\sim 0.75 \text{ pc}$.

The separations between two nearby fragments are counted from center to center with an average of $\sim 0.47 \pm 0.15 \text{ pc}$ (range in $\sim 0.21 - 0.65 \text{ pc}$). Considering the possible effect of projection, the separations would be $2/\pi$ times of the 3D ones on average (Sanhueza et al. 2019). And the possible 3D separations are $\sim 0.33 - 1.02 \text{ pc}$ with an average of $\sim 0.74 \pm 0.23 \text{ pc}$, which favors turbulent support rather than thermal support. It is worth noting that the popular-used spacing equation $L \simeq 22H$ with $H = \sigma\sqrt{4\pi G\rho_c}$ is under the condition of $\gamma = 0$ (i.e. ignorance of the magnetic field). Though Equation 7 cares about the magnetic field, it is under a helicoidal magnetic field assumption. For G16.96+0.27, we have no evidence of a helicoidal magnetic field, thus the result of L is for reference only.

4.3. Multiscale Cloud-field Alignment

As mentioned in Section 3, the $\sim 0.13 \text{ pc}$ scale magnetic field shows rough agreement with the $\sim 2.6 \text{ pc}$ -scale one but with some discrepancies in high-density regions. For further analysis, we use the histogram of relative orientations (HROs, Soler et al. 2013, 2017) method.

The HRO parameter ξ is defined as

$$\xi = \frac{A_0 - A_{90}}{A_0 + A_{90}}, \quad (9)$$

where A_0 and A_{90} represent the areas under the histogram of Φ (the angle between the POS magnetic field orientation and the iso-column density structure) value from 0° to 22.5° and 67.5° to 90° , respectively. While the derivation of ξ completely ignores angles from 22.5° to 67.5° , Jow et al. (2018) improved the HRO analysis with projected Rayleigh statistic (PRS) to overcome the shortcoming. Thus, we also use the normalized version of PRS, the alignment measure (AM) parameter (Lazarian et al. 2018; Liu et al. 2022) to study the relative alignment. The AM parameter is defined as

$$\text{AM} = \langle \cos 2\delta_\theta \rangle, \quad (10)$$

where δ_θ represents the relative orientation angle between the magnetic field and gas structure. A positive value of AM and ξ means the magnetic field tends to be parallel with $N(\text{H}_2)$ contour while a negative value stands for a perpendicular alignment.

We use POL-2 magnetic field ($14.4''$) data and $N(\text{H}_2)$ from the J-comb algorithm ($18''$) to calculate the small-scale AM and ξ . For the large-scale ones, we derive the column density by $\tau_{353}/N(\text{H}) = 1.2 \times 10^{-26} \text{cm}^{-2}$ to match the *Planck* 353 GHz magnetic field data, where τ_{353} is *Planck* 353 GHz dust optical depth (Planck Collaboration Int. XI et al. 2014). We mask regions with galactic latitude lower than 0.185° to avoid the effect of the emission from the Galactic plane.

As shown in the right panel of Figure 5, AM and ξ exhibit the same behavior with the increasing $N(\text{H}_2)$. They go from positive to negative at large-scale (red curve, low $N(\text{H}_2)$ traced by *Planck* data) but have the opposite behavior at small-scale (blue curve, high $N(\text{H}_2)$ traced by *Herschel*), showing a positive slope.

The behavior of AM and ξ indicates the following cloud-field alignment phenomenon. In the diffuse environment (with a $N(\text{H}_2)$ of $\sim 5.0 \times 10^{21} \text{cm}^{-2}$, shown in light-blue in the left panel of Figure 5), the magnetic field tends to be parallel with the gas structure. In the host structure (with a $N(\text{H}_2)$ of $\sim 1.3 \times 10^{22} \text{cm}^{-2}$, shown in green in the left panel of Figure 5), the magnetic field turns to be perpendicular to the gas structure, which is perpendicular to the galactic plane and extends to the northwest conjunct with M16, an active high-mass star-forming cloud (e.g. Hester et al. 1996; Sugitani et al. 2002; Pattle et al. 2018). In the outskirts (with a $N(\text{H}_2)$ of $\sim 2.5 \times 10^{22} \text{cm}^{-2}$) of the main structure (the middle panel of Figure 5), the alignment keeps perpendicular as in the host structure. In the dense center (with a $N(\text{H}_2)$

higher than $\sim 3.2 \times 10^{22} \text{cm}^{-2}$), it goes to be $\sim 45^\circ$ and shows a possible trend to be closer to parallelism.

Along the filament, we average the magnetic field orientation and skeleton orientation using a $32''$ filter, as $32''$ ($\sim 0.29 \text{pc}$) is similar to the diameter of the filament, and calculate δ_θ between them. As shown in the lower panel of Figure 4, regions beyond points SE and NW have few magnetic field segments and substantial uncertainties on δ_θ , so we mainly discuss the skeleton in-between. δ_θ shows fluctuations along the skeleton, it is $\sim 65\text{--}80^\circ$ at both ends, but becomes $\sim 40\text{--}50^\circ$ at the center. The behavior of δ_θ indicates that the local magnetic field tends to be perpendicular to the filament at the two diffuse ends but shows a trend to have a smaller offset with the filament at the dense center, which agrees with the behavior of AM and ξ shown in Figure 5.

Pillai et al. (2020) found a similar positive slope of ξ in dense regions of the hub-filament system Serpens South, suggesting the gas filaments merging into the central hub and reorienting the magnetic field in the dense gas flows. Kwon et al. (2022) found that ξ of Serpens Main shows large fluctuations with increasing $N(\text{H}_2)$, which is interpreted as the density gradient along the elongated structures becoming significant and magnetic field being dragged along with the increasing density. Furthermore, in the massive IRDC G28.34 (the Dragon cloud), Liu et al. (2024) found that the AM parameter also goes from negative to positive with increasing $N(\text{H}_2)$, and fluctuates around 0 in the very dense region traced by ALMA, suggesting G28.34 is located in a trans-to-sub-Alfvénic environment.

However, compared to Serpens South, Serpens Main and G28.34, G16.96+0.27 has a much simpler structure and less star-formation activity. As shown in the upper panel of Figure 1, MM1 and MM6 are not connected with the main structure from the infrared view, and most of the rest (MM3-MM5) are still starless cores. All the fragments have an average POS separation of $\sim 0.47 \text{pc}$, which may favor turbulent-supported fragmentation rather than thermal-supported one (see the discussion in Section 4.2). These results may indicate the following phenomenon: The G16.96+0.27 filament as a whole is quiescent and in quasi-equilibrium as reflected by the dark infrared morphology shown in Figure 1 and $M_l/M_{\text{crit},l}$ value. However, in the center region, the star formation process may have already begun as reflected by the fragments shown in Figure 1 and discussion in Section 4.2. Thus gravity has overcome the support of the magnetic field and turbulence, and dragged the field lines to align with the filament structure as has been observed at smaller scales in different targets (e.g., Sanhueza et al. 2021; Cortes et al. 2024).

Further, higher-resolution observations toward the center region are needed to investigate whether AM and ξ would fluctuate around 0 like G28.34 (Liu et al. 2024) or turn around showing the decreasing trend seen in the very dense regions ($N(\text{H}_2) \geq 1.6 \times 10^{23} \text{ cm}^{-2}$) in Serpens Main (Kwon et al. 2022).

5. SUMMARY

In this paper, we have presented the JCMT/POL-2 polarization observations towards an IRDC, G16.96+0.27, and the main conclusions are as follows:

(1) The average magnetic field orientation traced by JCMT/POL-2 is $\sim 60^\circ$, and a significant number of magnetic field segments exhibit a perpendicular alignment with the filament structure of G16.96+0.27, with an average angle difference of $\sim 66^\circ$. This result is consistent with the larger-scale magnetic field orientations traced by *Planck* 353 GHz data. The POS magnetic field strength is estimated to be $B_{\text{pos,dcf}} \sim 96 \mu\text{G}$ and $B_{\text{pos,adf}} \sim 60 \mu\text{G}$ using the classical DCF method and the ADF method, with an average strength of $\sim 78 \mu\text{G}$.

(2) The virial parameter and magnetic stability critical parameter are calculated as $\alpha_{\text{vir}} \sim 0.48$, $\lambda \sim 2.56$ with $\lambda_{\text{min}} \sim 0.86$, respectively. And the estimated ($M_l/M_{\text{critc},l}$) is ~ 1 , indicating that G16.96+0.27 is in a quasi-equilibrium state, but is more likely to be a gravitationally bound status when considering the magnetic field could be overestimated.

(3) We calculate the HRO parameter ξ and AM parameter based on *Planck* and JCMT data to study multiscale cloud-field alignment. With increasing $N(\text{H}_2)$, they first go across 0 to a negative minimum and then move back to 0. Along the filament, we apply the Fil-Finder algorithm to identify the skeleton of G16.96+0.27 and find that the local cloud-field alignment varies along the filament. The alignment is perpendicular at both diffuse ends but turns to be $\sim 45^\circ$ at the dense center, which is consistent with the behavior of AM and ξ . We also find that the observed separations among the fragments are in agreement with the predicted spacing from the ‘sausage’ instability theory under turbulent support assumption (Appendix 4.2). These results may reflect that although G16.96+0.27 is in quasi-equilibrium overall, fragmentation has already begun in the center of the filament, and such a phenomenon of cloud-field alignment inside IRDCs may be a possible sign of an early stage of star formation activity.

ACKNOWLEDGEMENTS

This work has been supported by the National Key R&D Program of China (No. 2022YFA1603100), Shanghai Rising-Star Program (23YF1455600), and Natural Science Foundation of Shanghai (No. 23ZR1482100). T.L. acknowledges support from the National Natural Science Foundation of China (NSFC), through grants No. 12073061 and No. 12122307, the Tianchi Talent Program of Xinjiang Uygur Autonomous Region, and the international partnership program of the Chinese Academy of Sciences, through grant No. 114231KYSB20200009. X.L. acknowledges support from the NSFC through grant Nos. 12273090 and 12322305, and the Chinese Academy of Sciences (CAS) ‘‘Light of West China’’ Program No. xbzg-zdsys-202212. MJ acknowledges the support of the Research Council of Finland Grant No. 348342. C.W.L. acknowledges support from the Basic Science Research Program through the NRF funded by the Ministry of Education, Science and Technology (NRF-2019R1A2C1010851) and by the Korea Astronomy and Space Science Institute grant funded by the Korea government (MSIT; project No. 2024-1-841-00). W.K. was supported by the National Research Foundation of Korea (NRF) grant funded by the Korea government (MSIT; project No. RS-2024-00342488). K.P. is a Royal Society University Research Fellow, supported by grant number URF\R1\211322. PS was partially supported by a Grant-in-Aid for Scientific Research (KAKENHI Number JP22H01271 and JP23H01221) of JSPS.

The James Clerk Maxwell Telescope is operated by the East Asian Observatory on behalf of The National Astronomical Observatory of Japan; Academia Sinica Institute of Astronomy and Astrophysics; the Korea Astronomy and Space Science Institute; the National Astronomical Research Institute of Thailand; Center for Astronomical Mega-Science (as well as the National Key R&D Program of China with No. 2017YFA0402700). Additional funding support is provided by the Science and Technology Facilities Council of the United Kingdom and participating universities and organizations in the United Kingdom and Canada. Additional funds for the construction of SCUBA-2 were provided by the Canada Foundation for Innovation.

Software: Astropy (Astropy Collaboration et al. 2013, 2018), FilFinder (Koch & Rosolowsky 2015)

APPENDIX

A. DATA REDUCTION PROCEDURES OF JCMT/POL-2 DATA

As the polarization fraction is forced to be positive, a bias is thus introduced (Vaillancourt 2006), and the

therefore debiased polarized intensity (PI) and corre-

sponding uncertainty (δ_{PI}) are calculated from

$$PI = \sqrt{Q^2 + U^2 - 0.5(\delta_Q^2 + \delta_U^2)}, \quad (\text{A1})$$

and

$$\delta_{PI} = \sqrt{\frac{Q^2\delta_Q^2 + U^2\delta_U^2}{Q^2 + U^2}}, \quad (\text{A2})$$

where δ_Q and δ_U are the uncertainties of Q and U . The debiased polarization fraction (p) and corresponding uncertainty (δ_p) are then derived by

$$p = PI/I, \quad (\text{A3})$$

and

$$\delta_p = \sqrt{\frac{\delta_{PI}^2}{I^2} + \frac{PI^2\delta_I^2}{I^4}}, \quad (\text{A4})$$

where δ_I is the uncertainty of I . Next, polarization angle (θ) and corresponding uncertainty (δ_θ) are calculated (Naghizadeh-Khouei & Clarke 1993) from

$$\theta = 0.5 \tan^{-1}(U/Q), \quad (\text{A5})$$

and

$$\delta_\theta = \frac{1}{2} \sqrt{\frac{Q^2\delta_U^2 + U^2\delta_Q^2}{(Q^2 + U^2)^2}}. \quad (\text{A6})$$

B. J-COMB ALGORITHM

We get the column density map by applying the J-comb algorithm (Jiao et al. 2022) based on level 2.5 processed, archival *Herschel* data and this JCMT 850 μm data, the main procedures are as follows:

1. Derive combined Stokes I map. We extrapolated an 850 μm flux map from the spectral energy distribution (SED) of *Herschel* 250/350/500 μm data using the

Spectral and Photometric Imaging REceiver (SPIRE; obsID: 1342228342; Griffin et al. 2010). Taking this map as a model image, we deconvolved the *Planck* 353 GHz map (Planck Collaboration Int. XIX et al. 2011) with the Lucy-Richardson algorithm (Lucy 1974). The obtained deconvolved map has an angular resolution close to the SPIRE 500 μm data and preserves the flux level of the initial *Planck* map. Then the combined Stokes I map (as shown in Figure 1 (a)) was generated via the J-comb algorithm (Jiao et al. 2022) by combining the deconvolved map with JCMT 850 μm Stokes I map in the Fourier domain.

2. SED fitting. We smoothed *Herschel* images at 70/160 μm using the Photodetector Array Camera and Spectrometer (obsID: 1342228372; Poglitsch et al. 2010), SPIRE 250 μm and the combined JCMT 850 μm Stokes I map to a common angular resolution of the largest beam. We weighted the data points by the measured noise level in the least-squares fits. As a modified black-body assumption, the flux density S_ν at the frequency ν is given by

$$S_\nu = \Omega_m B_\nu(T)(1 - e^{-\tau_\nu}), \quad (\text{B7})$$

where Ω_m is the solid angle, $B_\nu(T)$ is the Planck function at temperature T_{dust} . Then the column density is derived from

$$N(\text{H}_2) = \tau_\nu / \kappa_\nu \mu m_{\text{H}}, \quad (\text{B8})$$

where $\kappa_\nu = 0.1 \text{cm}^2 \text{g}^{-1} (\nu / 1000 \text{GHz})^\beta$ is the dust opacity assuming a gas-to-dust ratio of 100 and an opacity index β of 2 (Hildebrand 1983; Beckwith et al. 1990), $\mu = 2.8$ is the molecular weight per hydrogen molecule (Kauffmann et al. 2008), and m_{H} is the atomic mass of hydrogen.

REFERENCES

- André, P., Di Francesco, J., Ward-Thompson, D., et al. 2014, in *Protostars and Planets VI*, ed. H. Beuther, R. S. Klessen, C. P. Dullemond, & T. Henning, 27–51, doi: [10.2458/azu_uapress.9780816531240-ch002](https://doi.org/10.2458/azu_uapress.9780816531240-ch002)
- André, P., Men'shchikov, A., Bontemps, S., et al. 2010, *A&A*, 518, L102, doi: [10.1051/0004-6361/201014666](https://doi.org/10.1051/0004-6361/201014666)
- Arzoumanian, D., André, P., Didelon, P., et al. 2011, *A&A*, 529, L6, doi: [10.1051/0004-6361/201116596](https://doi.org/10.1051/0004-6361/201116596)
- Astropy Collaboration, Robitaille, T. P., Tollerud, E. J., et al. 2013, *A&A*, 558, A33, doi: [10.1051/0004-6361/201322068](https://doi.org/10.1051/0004-6361/201322068)
- Astropy Collaboration, Price-Whelan, A. M., Sipőcz, B. M., et al. 2018, *AJ*, 156, 123, doi: [10.3847/1538-3881/aabc4f](https://doi.org/10.3847/1538-3881/aabc4f)
- Beckwith, S. V. W., Sargent, A. I., Chini, R. S., & Guesten, R. 1990, *AJ*, 99, 924, doi: [10.1086/115385](https://doi.org/10.1086/115385)
- Chandrasekhar, S., & Fermi, E. 1953a, *ApJ*, 118, 113, doi: [10.1086/145731](https://doi.org/10.1086/145731)
- . 1953b, *ApJ*, 118, 116, doi: [10.1086/145732](https://doi.org/10.1086/145732)
- Chapin, E. L., Berry, D. S., Gibb, A. G., et al. 2013, *MNRAS*, 430, 2545, doi: [10.1093/mnras/stt052](https://doi.org/10.1093/mnras/stt052)
- Ching, T.-C., Qiu, K., Li, D., et al. 2022, *ApJ*, 941, 122, doi: [10.3847/1538-4357/ac9dfb](https://doi.org/10.3847/1538-4357/ac9dfb)
- Cho, J., & Yoo, H. 2016, *ApJ*, 821, 21, doi: [10.3847/0004-637X/821/1/21](https://doi.org/10.3847/0004-637X/821/1/21)
- Contreras, Y., Garay, G., Rathborne, J. M., & Sanhueza, P. 2016, *MNRAS*, 456, 2041, doi: [10.1093/mnras/stv2796](https://doi.org/10.1093/mnras/stv2796)

- Cortes, P. C., Girart, J. M., Sanhueza, P., et al. 2024, arXiv e-prints, arXiv:2406.14663, doi: [10.48550/arXiv.2406.14663](https://doi.org/10.48550/arXiv.2406.14663)
- Crutcher, R. M. 2012, *ARA&A*, 50, 29, doi: [10.1146/annurev-astro-081811-125514](https://doi.org/10.1146/annurev-astro-081811-125514)
- Crutcher, R. M., Nutter, D. J., Ward-Thompson, D., & Kirk, J. M. 2004, *ApJ*, 600, 279, doi: [10.1086/379705](https://doi.org/10.1086/379705)
- Currie, M. J., Berry, D. S., Jenness, T., et al. 2014, in *Astronomical Society of the Pacific Conference Series*, Vol. 485, *Astronomical Data Analysis Software and Systems XXIII*, ed. N. Manset & P. Forshay, 391
- Davis, L. 1951, *Physical Review*, 81, 890, doi: [10.1103/PhysRev.81.890.2](https://doi.org/10.1103/PhysRev.81.890.2)
- Falceta-Gonçalves, D., Lazarian, A., & Kowal, G. 2008, *ApJ*, 679, 537, doi: [10.1086/587479](https://doi.org/10.1086/587479)
- Fiege, J. D., & Pudritz, R. E. 2000, *MNRAS*, 311, 105, doi: [10.1046/j.1365-8711.2000.03067.x](https://doi.org/10.1046/j.1365-8711.2000.03067.x)
- Friberg, P., Bastien, P., Berry, D., et al. 2016, *Proc. SPIE*, 9914, 991403, doi: [10.1117/12.2231943](https://doi.org/10.1117/12.2231943)
- Friberg, P., Berry, D., Savini, G., et al. 2018, *Proc. SPIE*, 10708, 107083M, doi: [10.1117/12.2314345](https://doi.org/10.1117/12.2314345)
- Griffin, M. J., Abergel, A., Abreu, A., et al. 2010, *A&A*, 518, L3, doi: [10.1051/0004-6361/201014519](https://doi.org/10.1051/0004-6361/201014519)
- Gu, Q.-L., Liu, T., Li, P. S., et al. 2024, *ApJ*, 963, 126, doi: [10.3847/1538-4357/ad1bc7](https://doi.org/10.3847/1538-4357/ad1bc7)
- Hester, J. J., Scowen, P. A., Sankrit, R., et al. 1996, *AJ*, 111, 2349, doi: [10.1086/117968](https://doi.org/10.1086/117968)
- Hildebrand, R. H. 1983, *QJRAS*, 24, 267
- Hildebrand, R. H., Kirby, L., Dotson, J. L., Houde, M., & Vaillancourt, J. E. 2009, *ApJ*, 696, 567, doi: [10.1088/0004-637X/696/1/567](https://doi.org/10.1088/0004-637X/696/1/567)
- Holland, W. S., Bintley, D., Chapin, E. L., et al. 2013, *MNRAS*, 430, 2513, doi: [10.1093/mnras/sts612](https://doi.org/10.1093/mnras/sts612)
- Houde, M., Hull, C. L. H., Plambeck, R. L., Vaillancourt, J. E., & Hildebrand, R. H. 2016, *ApJ*, 820, 38, doi: [10.3847/0004-637X/820/1/38](https://doi.org/10.3847/0004-637X/820/1/38)
- Houde, M., Vaillancourt, J. E., Hildebrand, R. H., Chitsazzadeh, S., & Kirby, L. 2009, *ApJ*, 706, 1504, doi: [10.1088/0004-637X/706/2/1504](https://doi.org/10.1088/0004-637X/706/2/1504)
- Inutsuka, S.-I., & Miyama, S. M. 1992, *ApJ*, 388, 392, doi: [10.1086/171162](https://doi.org/10.1086/171162)
- Jiao, S., Lin, Y., Shui, X., et al. 2022, *Science China Physics, Mechanics, and Astronomy*, 65, 299511, doi: [10.1007/s11433-021-1902-3](https://doi.org/10.1007/s11433-021-1902-3)
- Jow, D. L., Hill, R., Scott, D., et al. 2018, *MNRAS*, 474, 1018, doi: [10.1093/mnras/stx2736](https://doi.org/10.1093/mnras/stx2736)
- Kashiwagi, R., & Tomisaka, K. 2021, *ApJ*, 911, 106, doi: [10.3847/1538-4357/abea7a](https://doi.org/10.3847/1538-4357/abea7a)
- Kauffmann, J., Bertoldi, F., Bourke, T. L., Evans, N. J., I., & Lee, C. W. 2008, *A&A*, 487, 993, doi: [10.1051/0004-6361:200809481](https://doi.org/10.1051/0004-6361:200809481)
- Kim, G., Tatematsu, K., Liu, T., et al. 2020, *ApJS*, 249, 33, doi: [10.3847/1538-4365/aba746](https://doi.org/10.3847/1538-4365/aba746)
- Koch, E. W., & Rosolowsky, E. W. 2015, *MNRAS*, 452, 3435, doi: [10.1093/mnras/stv1521](https://doi.org/10.1093/mnras/stv1521)
- Könyves, V., André, P., Men'shchikov, A., et al. 2015, *A&A*, 584, A91, doi: [10.1051/0004-6361/201525861](https://doi.org/10.1051/0004-6361/201525861)
- Kwon, W., Pattle, K., Sadavoy, S., et al. 2022, *ApJ*, 926, 163, doi: [10.3847/1538-4357/ac4bbe](https://doi.org/10.3847/1538-4357/ac4bbe)
- Lazarian, A. 2003, *JQSRT*, 79-80, 881, doi: [10.1016/S0022-4073\(02\)00326-6](https://doi.org/10.1016/S0022-4073(02)00326-6)
- Lazarian, A., Yuen, K. H., Ho, K. W., et al. 2018, *ApJ*, 865, 46, doi: [10.3847/1538-4357/aa7ff](https://doi.org/10.3847/1538-4357/aa7ff)
- Li, H. B., Goodman, A., Sridharan, T. K., et al. 2014, in *Protostars and Planets VI*, ed. H. Beuther, R. S. Klessen, C. P. Dullemond, & T. Henning, 101–123, doi: [10.2458/azu_uapress.9780816531240-ch005](https://doi.org/10.2458/azu_uapress.9780816531240-ch005)
- Li, H.-B., Yuen, K. H., Otto, F., et al. 2015, *Nature*, 520, 518, doi: [10.1038/nature14291](https://doi.org/10.1038/nature14291)
- Li, P. S., & Klein, R. I. 2019, *MNRAS*, 485, 4509, doi: [10.1093/mnras/stz653](https://doi.org/10.1093/mnras/stz653)
- Liu, H. B., Jiménez-Serra, I., Ho, P. T. P., et al. 2012, *ApJ*, 756, 10, doi: [10.1088/0004-637X/756/1/10](https://doi.org/10.1088/0004-637X/756/1/10)
- Liu, J., Qiu, K., & Zhang, Q. 2022, *ApJ*, 925, 30, doi: [10.3847/1538-4357/ac3911](https://doi.org/10.3847/1538-4357/ac3911)
- Liu, J., Zhang, Q., Commerçon, B., et al. 2021, *ApJ*, 919, 79, doi: [10.3847/1538-4357/ac0cec](https://doi.org/10.3847/1538-4357/ac0cec)
- Liu, J., Zhang, Q., Lin, Y., et al. 2024, *ApJ*, 966, 120, doi: [10.3847/1538-4357/ad3105](https://doi.org/10.3847/1538-4357/ad3105)
- Liu, T., Li, P. S., Juvela, M., et al. 2018a, *ApJ*, 859, 151, doi: [10.3847/1538-4357/aac025](https://doi.org/10.3847/1538-4357/aac025)
- Liu, T., Kim, K.-T., Juvela, M., et al. 2018b, *ApJS*, 234, 28, doi: [10.3847/1538-4365/aaa3dd](https://doi.org/10.3847/1538-4365/aaa3dd)
- Lu, X., Zhang, Q., Liu, H. B., et al. 2018, *ApJ*, 855, 9, doi: [10.3847/1538-4357/aaad11](https://doi.org/10.3847/1538-4357/aaad11)
- Lucy, L. B. 1974, *AJ*, 79, 745, doi: [10.1086/111605](https://doi.org/10.1086/111605)
- Mairs, S., Dempsey, J. T., Bell, G. S., et al. 2021, *AJ*, 162, 191, doi: [10.3847/1538-3881/ac18bf](https://doi.org/10.3847/1538-3881/ac18bf)
- Mannfors, E., Juvela, M., Bronfman, L., et al. 2021, *A&A*, 654, A123, doi: [10.1051/0004-6361/202037791](https://doi.org/10.1051/0004-6361/202037791)
- Morii, K., Sanhueza, P., Nakamura, F., et al. 2023, *ApJ*, 950, 148, doi: [10.3847/1538-4357/accea](https://doi.org/10.3847/1538-4357/accea)
- Myers, P. C. 2009, *ApJ*, 700, 1609, doi: [10.1088/0004-637X/700/2/1609](https://doi.org/10.1088/0004-637X/700/2/1609)
- Naghizadeh-Khouei, J., & Clarke, D. 1993, *A&A*, 274, 968
- Nakamura, F., Hanawa, T., & Nakano, T. 1993, *PASJ*, 45, 551

- Ostriker, E. C., Stone, J. M., & Gammie, C. F. 2001, *ApJ*, 546, 980, doi: [10.1086/318290](https://doi.org/10.1086/318290)
- Pattle, K., Fissel, L., Tahani, M., Liu, T., & Ntormousi, E. 2023, in *Astronomical Society of the Pacific Conference Series*, Vol. 534, *Protostars and Planets VII*, ed. S. Inutsuka, Y. Aikawa, T. Muto, K. Tomida, & M. Tamura, 193, doi: [10.48550/arXiv.2203.11179](https://doi.org/10.48550/arXiv.2203.11179)
- Pattle, K., Ward-Thompson, D., Hasegawa, T., et al. 2018, *ApJL*, 860, L6, doi: [10.3847/2041-8213/aac771](https://doi.org/10.3847/2041-8213/aac771)
- Pillai, T. G. S., Clemens, D. P., Reissl, S., et al. 2020, *Nature Astronomy*, 4, 1195, doi: [10.1038/s41550-020-1172-6](https://doi.org/10.1038/s41550-020-1172-6)
- Planck Collaboration Int. XI, Abergel, A., Ade, P. A. R., et al. 2014, *A&A*, 571, A11, doi: [10.1051/0004-6361/201323195](https://doi.org/10.1051/0004-6361/201323195)
- Planck Collaboration Int. XIX, Ade, P. A. R., Aghanim, N., et al. 2011, *A&A*, 536, A19, doi: [10.1051/0004-6361/201116479](https://doi.org/10.1051/0004-6361/201116479)
- Planck Collaboration Int. XXXV, Ade, P. A. R., Aghanim, N., et al. 2016, *A&A*, 586, A138, doi: [10.1051/0004-6361/201525896](https://doi.org/10.1051/0004-6361/201525896)
- Poglitsch, A., Waelkens, C., Geis, N., et al. 2010, *A&A*, 518, L2, doi: [10.1051/0004-6361/201014535](https://doi.org/10.1051/0004-6361/201014535)
- Sanhueza, P., Contreras, Y., Wu, B., et al. 2019, *ApJ*, 886, 102, doi: [10.3847/1538-4357/ab45e9](https://doi.org/10.3847/1538-4357/ab45e9)
- Sanhueza, P., Girart, J. M., Padovani, M., et al. 2021, *ApJL*, 915, L10, doi: [10.3847/2041-8213/ac081c](https://doi.org/10.3847/2041-8213/ac081c)
- Soam, A., Liu, T., Andersson, B. G., et al. 2019, *ApJ*, 883, 95, doi: [10.3847/1538-4357/ab39dd](https://doi.org/10.3847/1538-4357/ab39dd)
- Soler, J. D., Hennebelle, P., Martin, P. G., et al. 2013, *ApJ*, 774, 128, doi: [10.1088/0004-637X/774/2/128](https://doi.org/10.1088/0004-637X/774/2/128)
- Soler, J. D., Ade, P. A. R., Angilè, F. E., et al. 2017, *A&A*, 603, A64, doi: [10.1051/0004-6361/201730608](https://doi.org/10.1051/0004-6361/201730608)
- Sugitani, K., Tamura, M., Nakajima, Y., et al. 2002, *ApJL*, 565, L25, doi: [10.1086/339196](https://doi.org/10.1086/339196)
- Tafalla, M., & Hacar, A. 2015, *A&A*, 574, A104, doi: [10.1051/0004-6361/201424576](https://doi.org/10.1051/0004-6361/201424576)
- Tang, Y.-W., Koch, P. M., Peretto, N., et al. 2019, *ApJ*, 878, 10, doi: [10.3847/1538-4357/ab1484](https://doi.org/10.3847/1538-4357/ab1484)
- Tatematsu, K., Kim, G., Liu, T., et al. 2021, *ApJS*, 256, 25, doi: [10.3847/1538-4365/ac0978](https://doi.org/10.3847/1538-4365/ac0978)
- Vaillancourt, J. E. 2006, *PASP*, 118, 1340, doi: [10.1086/507472](https://doi.org/10.1086/507472)
- Wang, K., Zhang, Q., Testi, L., et al. 2014, *MNRAS*, 439, 3275, doi: [10.1093/mnras/stu127](https://doi.org/10.1093/mnras/stu127)
- Zhang, Q., Wang, Y., Pillai, T., & Rathborne, J. 2009, *ApJ*, 696, 268, doi: [10.1088/0004-637X/696/1/268](https://doi.org/10.1088/0004-637X/696/1/268)